



Buoyancy-driven dissolution of inclined blocks: Erosion rate and pattern formation

Caroline Cohen, Michael Berhanu, Julien Derr , and Sylvain Courrech du Pont ^{*}
*Laboratoire Matières et Systèmes Complexes, Université de Paris, CNRS, and Bâtiment Condorcet,
10 rue Alice Domon et Léonie Duquet, 75205 Paris Cedex 13, France*



(Received 17 December 2019; accepted 21 April 2020; published 18 May 2020;
corrected 7 October 2020)

The dissolution of a body into quiescent water leads to density stratifications at the interfaces that drive buoyant flows. Where the stratification is unstable, the flow destabilizes into convective solute plumes. By analogy with the Rayleigh-Bénard instability where concentration replaces temperature, this phenomenon is known as the solutal Rayleigh-Bénard instability. Here we report experiments of the dissolution of inclined rectangular blocks made of salt, caramel, or plaster in aqueous solutions of various concentrations. The solute flows along the block while forming plumes before they detach and sink. This flow along the block organizes the emission of plumes within longitudinal parallel stripes with a well-defined millimeter-scale wavelength. The instability of the flow reflects on the concentration field in the boundary layer, which engraves longitudinal grooves onto the block. These grooves interact with the flow and turn into a paving of three-dimensional, cuplike patterns that grow in size and propagate upstream. These bedforms are reminiscent of the scallop bedforms observed on the walls of cave or icebergs. Whereas the block interface is highly dynamical and evolves through time, it remains flat on the global scale and recedes at a stationary rate. We derive scaling laws for the receding velocity and the pattern genesis at the inclined interface that are based on a concentration boundary layer of constant thickness, which is controlled by the flow instability but where neither the patterns nor the flow along the block play any role. We apply these results to the formation of sublimation patterns.

DOI: [10.1103/PhysRevFluids.5.053802](https://doi.org/10.1103/PhysRevFluids.5.053802)

I. INTRODUCTION

A water flow and its interaction with a topography modifies the rate of phase transition, dissolution, or precipitation of a body. In nature, the coupling between the geometry and the mass transfer drives the formation of recognizable patterns at different scales. These can be erosion patterns like river meanders, cyclic steps, rillenkarren, lapiaz, ice ripples, dissolution flutes and scallops, regmaglypts on meteorites, or deposition shapes like travertines, stalactites, icicles, or brinicles. These patterns are not geological curiosities only but are markers of the hydrodynamic processes, which often control the global erosion process. The identification of erosion and deposition patterns is therefore a key to infer flow and thermodynamic conditions. It is especially valuable because these structures are quite resilient and give information on the long term, not only for Earth but also for other planetary bodies that are difficult to instrument.

Here we study the dissolution of rectangular blocks immersed in still aqueous solutions in the case where the solute stratification it engenders is buoyancy unstable [1]. The concentration

^{*}sylvain.courrech@univ-paris-diderot.fr

boundary layer destabilizes to form plumes that drive a convective flow of solute. This heterogeneous flow influences the concentration field at the interface, which patterns the dissolving body.

Several studies address the growth or dissolution of solids into aqueous solutions and the subsequent turbulent solutal convective flow [2–10]. Most of them do the parallel with the Rayleigh-Bénard instability, where the buoyancy is not due to the thermal expansion of the liquid but to the gradients of solute concentration. These studies are either motivated by industrial applications from a chemical engineering perspective [5,6] or by geophysical questions such as the sequestration of CO₂ in porous rocks [11–14] or the formation of patterns like brinicles or corrugations on the ice cap of brackish lakes or in magma chambers [7,8,15–17].

Our experimental study stands out from these previous studies by addressing the dissolution of inclined blocks. The inclination of the block gives a direction to the dissolution flow. As a result, the instability of the flow and the primary patterns are longitudinal with a well-defined wavelength. The latter interplay between the dissolution flow and the shaped topography gives rise to dynamical three-dimensional structures that propagate upstream the dissolution flow. In the next section (Sec. II) we detail our experiments with caramel, salt or plaster blocks, which are fast dissolving materials. The caramel being transparent, we can follow the pattern formation in real time. In Sec. III we derive scaling laws for the dissolution rate and for the characteristic time and wavelength of pattern formation in the case of inclined bodies. We compare the scaling laws to the experimental data in Sec. IV. We show in particular that the solute flow along the block and the dynamics of patterns at the block interface have little if any influence on the global dissolution rate. Finally, we put our work in perspective in a geomorphological context. In Sec. V we make the connection between the dissolution and sublimation patterns such as penitentes. In conclusion, we link our work to the dissolution cavities observed in nature and compare the free dissolution patterns we observe in our experiments with their counterparts shaped by an externally imposed stream.

II. EXPERIMENTS

We investigate the dissolution of rectangular blocks of either caramel, salt (NaCl), or plaster (gypsum) immersed in quiescent aqueous solutions. We systematically vary the inclination of the block and the solute concentration of the solution.

Salt blocks come from Himalayan mines. They are typically 10 cm long, 5 cm wide, and 2.5 cm thick and have a density of $\rho_s = 2348 \pm 5 \text{ kg m}^{-3}$. We stick to blocks aluminum lugs with silicon sealant to hold them into the saline solution. We mix tap water and table salt to prepare solutions of various concentrations. The measured density of the saturated brine is $\rho_{\text{sat}} = 1197.3 \pm 1 \text{ kg m}^{-3}$ at 22°C. Caramel is made with saccharose, tap water, and a few drops of lemon juice (acid) to favor the caramelization reaction. We cast hot caramel into silicon molds of $10 \times 10 \times 3 \text{ cm}$ or $5.5 \times 2.5 \times 2 \text{ cm}$ to obtain rectangular blocks. An allen wrench is embedded in the block to hold it in the solution. The color of caramel is controlled during cooking to ensure that blocks are of similar properties and constant density ($\rho_s = 1540 \pm 10 \text{ kg m}^{-3}$). We either mix tap water and caramel or tap water and saccharose to prepare the syrups. The measured density of the saturated caramel solution is $\rho_{\text{sat}} = 1450 \pm 10 \text{ kg m}^{-3}$. We made the plaster block by pouring a $5.5 \times 2.5 \times 2 \text{ cm}$ silicon mold with a mix of fine powder of plaster of Paris and water. The density of the block is $\rho_s = 1859 \pm 5 \text{ kg m}^{-3}$, and we measured a density difference of $1.8 \pm 0.6 \text{ kg m}^{-3}$ between the saturated solution and water.

An experiment consists in immersing a block at room temperature (between 19°C and 24°C) at the center of a glass tank which is 40 cm long, 20 cm wide, and is filled with the solution to a depth of 20 cm. We capture the receding of the bottom and top interfaces with a camera (see Fig. 1). Caramel blocks are transparent so that we can also record the formation and the evolution of patterns on the bottom interface. To do so, we light the block from behind and either take pictures of the bottom interface thanks to an inclined mirror put into the tank or take frontal pictures with the camera positioned underneath and the tank tilted at the same angle as the immersed block (Fig. 2). We cannot observe the patterns on the salt and plaster blocks when immersed. They are opaque and

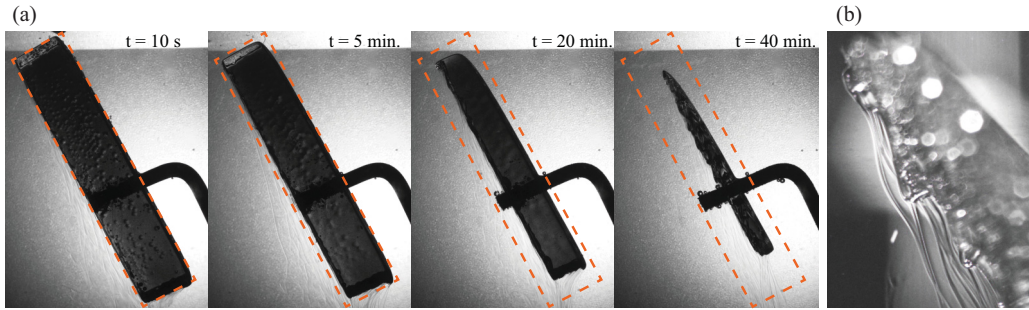


FIG. 1. (a) Side view of a caramel block dissolving into water. The initial block is 6 cm long and makes an angle of 62° with the horizontal. Except in the vicinity of the top corner, the overall inclination of the receding bottom interface does not change over time. On the contrary, the top interface dissolves faster at the top (upstream) than at the bottom (downstream). (b) Details showing solute threads detaching from tips at the bottom interface.

interfaces appear blurry because of the gradient of the solute concentration and consequently of the refractive index of the solution in the vicinity of interfaces. We take salt and plaster blocks out of solutions to observe the patterns.

Figures 1 and 2 show side views and bottom views of the evolution of an inclined caramel block immersed in water. The block dissolves, interfaces recede, and we observe different flows and block dynamics depending on the orientation of the block walls. Threads of solute-laden fluid escape from the block interfaces pointing downwards and sink while the solute flows all along the block walls pointing upwards (Fig. 3). The inclination of the block enforces a downward direction to the flow on either interface. On the bottom interface, the solute flows downwards before detaching

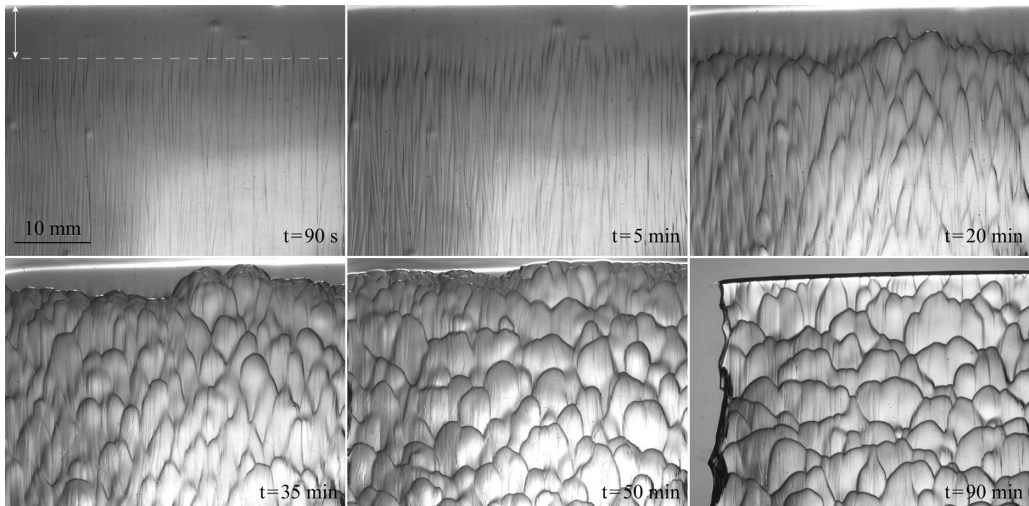


FIG. 2. Pattern formation. Bottom view of a caramel block dissolving into water. The block makes an angle of 60° with the horizontal. The top of the first picture corresponds to the block end. The block is lit from the back, crests and peaks appear dark. Parallel stripes rapidly form beyond an entry length from the block end. Then stripes cross and evolve into scallops that propagate upstream. The white dashed line and arrows show the entry length on the first picture. See Ref. [19] for a movie showing a time lapse of the pattern formation and evolution.

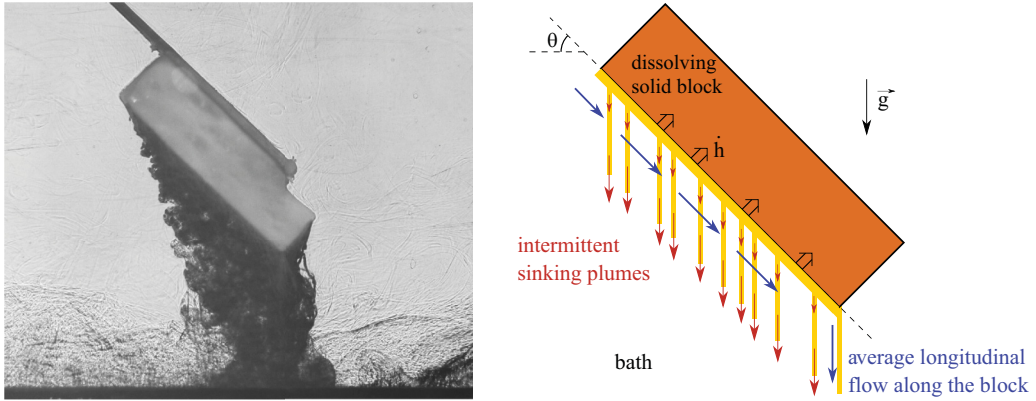


FIG. 3. Left: Schlieren picture of a salt block dissolving into water. The block is 9 cm long and makes an angle of 45° with the horizontal. One sees the very different solute flows on the interfaces facing upwards and downwards. On the bottom interface, the solute-laden fluid also flows along the block before detaching because the block is inclined. This flow has some inertia, as observed at the bottom corner of the block. One also sees that the solute-laden fluid poorly mixes with the bath solution but sinks and accumulates at the bottom of the tank. This picture is a snapshot of a movie that is available online, see Ref. [18]. Right: Schematic view of the dissolution-driven flow.

(see Fig. 3 and a supplementary movie, Ref. [18]). Using particle image velocimetry, we measured a typical along-block downward velocity of 1.5 cm/s at a distance of 10 mm beneath the bottom interface of a caramel block dissolving in water with an inclination of 60° and of 2 cm/s at a distance of 8 mm beneath a salt block dissolving in water with an inclination of 40° . The differences in solute transport depending on the orientation of the block interface go along with a different erosion velocity and shaping of the block walls. The block dissolves faster at interfaces facing downwards than at interfaces facing upwards. Moreover, while the walls facing upwards remain smooth, patterns form on the walls facing downwards. For the experiment shown in Fig. 2, longitudinal parallel stripes with an initial wavelength of 0.4 mm are observed a few seconds after immersion. These stripes extend on the whole length of the block after a given “entry” distance from the top. Then the wavelength increases with time, and longitudinal stripes evolve into chevrons and then into cuplike patterns named scallops by geologists, that propagate upwards, i.e., upstream. After an hour, scallops are 7.6 mm wide, 6.3 mm long, and propagate at a velocity of about 3×10^{-3} mm/s. They have the typical shape of rounded troughs and acute peaks with an asymmetry between the upstream and downstream sides. A movie of the pattern formation and evolution is available, see Ref. [19]. Although patterns grow, evolve, and propagate on the bottom interface, its overall inclination does not change over time (but in the vicinity of the top corner), and the global receding velocity is found remarkably constant through time, as shown in Fig. 4. A similar result is obtained in simulations of Rayleigh-Bénard convection with a melting boundary, which show a constant receding rate of the mean position of the boundary while patterns are growing [20].

Figure 5 shows the evolution of patterns at the bottom interface of a salt block when immersed into water. The dissolution scenario we described applies for all the dissolution experiments we performed. However, the characteristic time and length scales depend on material, initial bath concentration, or inclination of the block. We measure the initial wavelength of longitudinal stripes λ_s , the characteristic growth time T_s for their formation, and the global erosion velocity \dot{h} of the block wall pointing downwards for blocks of caramel or salt for different inclinations and concentrations of solutions and for one block of plaster into water. Figure 6 shows early longitudinal stripes observed on the bottom wall of caramel blocks immersed in syrups of different concentration. The initial wavelength as the characteristic time for their formation increases with the bath concentration.

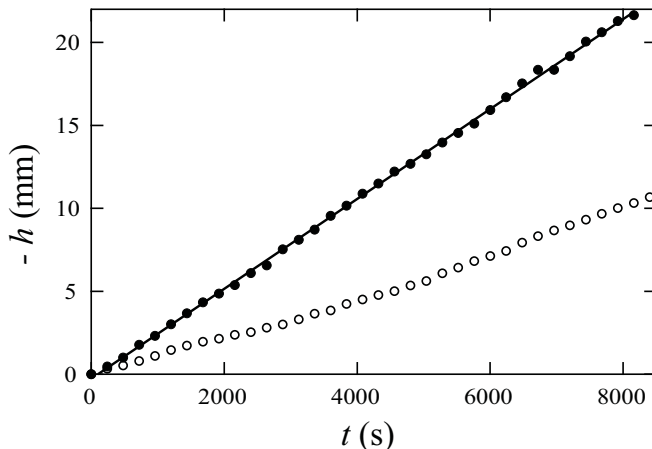


FIG. 4. Position h taken in the middle of the bottom interface (plain points) and of the top interface (empty points) as a function of time t for a caramel block making an angle of 62° with horizontal dissolving into water. The black line shows a linear fit. We measure positions along lines normal to the initial interfaces. We average the receding velocities from the measurements along five different lines along the block. The mean receding velocity of the bottom interface is $\dot{h} = -2.78 \times 10^{-3} \pm 3 \times 10^{-5}$ mm/s.

The interface recedes faster when the concentration of the bath solution is smaller. We also observe that the initial wavelength and growth time increase, and the interface recedes slower when the inclination angle of the block increases (see the Supplemental Material for tables and plots of the raw data [21]).

III. SCALING LAWS: A SOLUTAL RAYLEIGH-BÉNARD INSTABILITY

The rate of dissolution (or precipitation) of a solid block depends on the difference between the concentration of the solution at the block interface and the saturation concentration. The simplest yet reasonable dependency assumes a linear relationship with a constant characteristic dissolution (or precipitation) velocity, which contains the chemical kinetics [22,23]. The equation of conservation of the mass flux per unit of area reads

$$\rho_s \frac{\partial h}{\partial t} \vec{n} = \alpha (C_i - C_{\text{sat}}) \vec{n}, \quad (1)$$

where ρ_s is the density of the solid and α the characteristic dissolution velocity. C_i and C_{sat} are the mass concentrations of the solution at the interface and of the saturated solution, respectively. \vec{n} is a unit vector, normal to the solid interface.

For a flat and horizontal interface, if the dissolution process generates a density stratification that is buoyancy stable, only the diffusion drives the mass transport into the solution. Then, when putting a block in the solution, the concentration at the interface increases towards the saturation value on a characteristic time D/α^2 , where D is the coefficient of diffusion of the solute. The receding velocity of the dissolving block decreases with time, and for large times, the interface position withdraws as the square root of time [23].

If the dissolution process generates a density stratification that is buoyancy unstable, a completely different scenario occurs. When immersing the block, it starts dissolving and a front of dissolved medium moves away from the solid interface. On small lengths, close to the solid interface, the diffusion drives the transport. But beyond a characteristic length, the gravity takes over the transport. As a result, the concentration front destabilizes into plumes [24] (see Fig. 7). This instability is a solutal Rayleigh-Bénard instability where concentration replaces temperature and

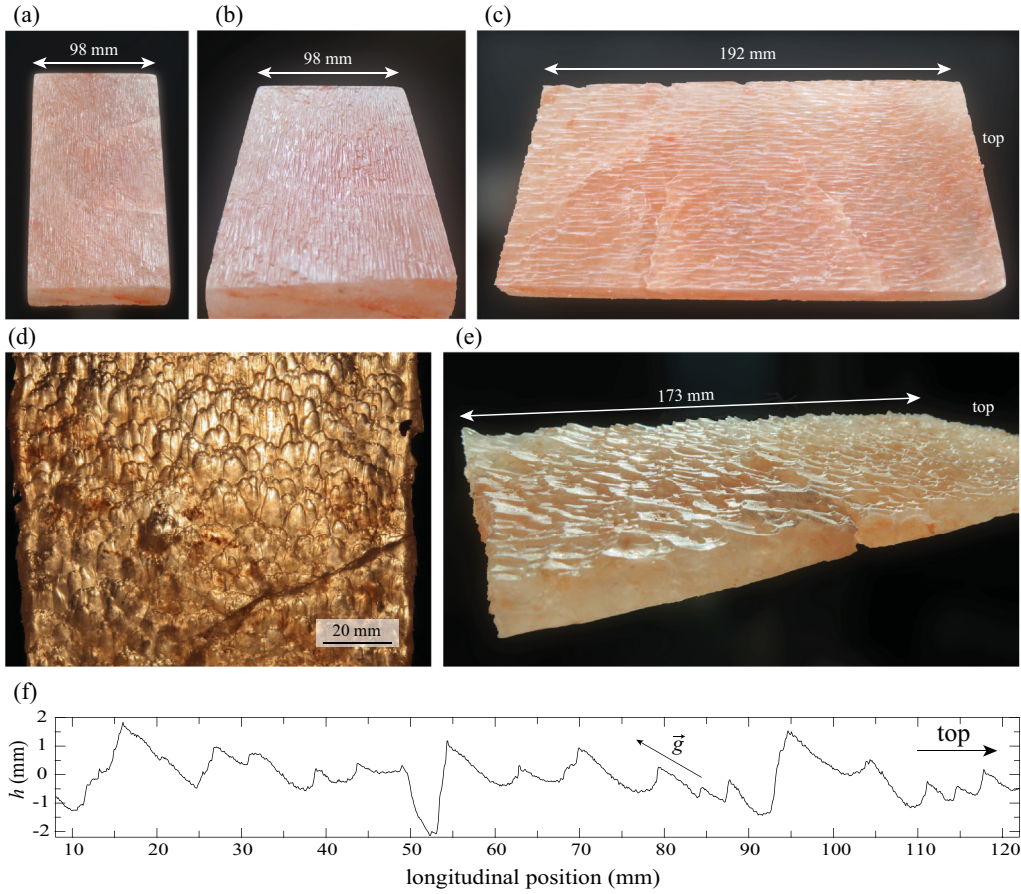


FIG. 5. Pattern formation. Bottom view of a salt block after 5 min (a), 10 min (b), 20 min (c), and 1 hour (d, e) of immersion into pure water with an inclination of 60° with the horizontal. Image (d) is lit from the back. Image (e) shows the asymmetry and pointy tips of dissolution patterns. Graphic (f) shows a line profile along this block. The slope on the stoss side seems parallel to the gravity in the vicinity of the tip. After an hour of immersion, the standard deviation of the topography is 0.62 mm.

the same scaling laws apply as previously observed by [2,7,9,15,25,26]. Identically, it can be seen as a Rayleigh-Taylor instability of a thin film whose thickness and concentration are controlled by diffusion [25,26]. In the classical Rayleigh-Taylor instability, the interface between two fluids of different density destabilizes when the heavier fluid is above the lighter one. The growth rate of perturbations is larger for small wavelengths. However, for nonmiscible fluids, surface tension prevents the shorter wavelengths from growing and the most unstable wavelength is given by the capillary length. For a thin film, when the surface tension goes to zero, the characteristic wavelength is given by the thickness of the film. Brown did the linear stability analysis in two dimensions (2D) for a horizontal thin film of a viscous liquid above an inviscid fluid and in contact with a solid wall at its upper limit [27]. The most unstable wavelength λ_f and its associated growth rate σ_f are [27,28]

$$\lambda_f \simeq 3\delta \quad \& \quad \sigma_f \simeq 0.32 \delta \Delta\rho g / \eta_f, \quad (2)$$

where δ is the thickness of the destabilizing film, $\Delta\rho$ the apparent density, η_f the dynamic viscosity of the fluid in the film, and g the gravity acceleration. In Brown calculation there is no diffusion nor tangential stress at the interface because the outer fluid is inviscid. This last simplification holds

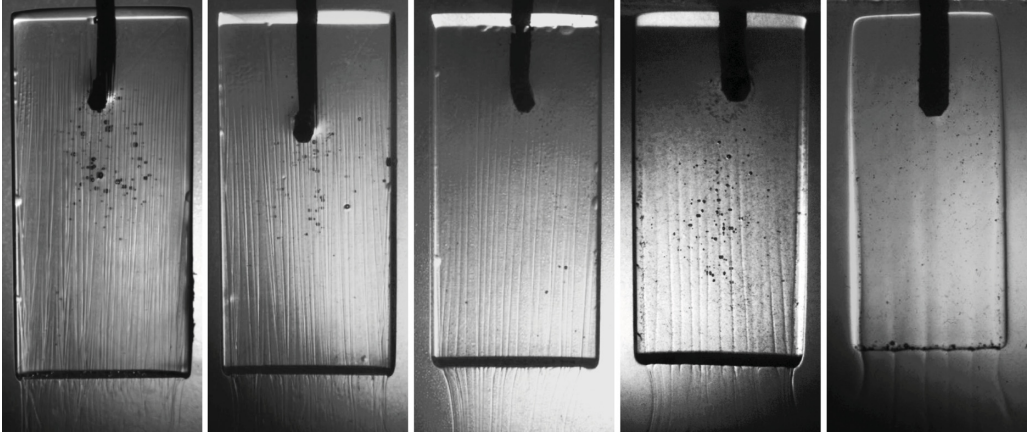


FIG. 6. Bottom view of caramel blocks (55×25 mm) dissolving into aqueous solutions of different caramel concentrations. From left to right, the densities of solutions are $\rho_b = 1006, 1108, 1229, 1303,$ and 1403 kg m^{-3} . The inclination of blocks ranges between 70° and 75° .

for a viscous outer fluid when its dynamic viscosity is small compared to that of the fluid in the thin film and/or when the wavelength is large compared to the thickness of the film. Lister and Kerr extended the calculation for two fluids of different finite viscosities [29]. For two fluids with equaled dynamic viscosities, they found $\lambda_f \simeq 3.8 \delta$ [29]. Hereafter, we denote R_λ the ratio between λ_f and δ . Naturally, σ_f scales as the inverse of the characteristic settling time of a particle of diameter δ in terminal Stokes velocity over a length equal to its diameter.

The front between the layer of dissolved medium and the solvent is unstable when the gravity overcomes the diffusion to transport the dissolved mass and concentration. Thus, the thickness δ of the destabilizing film is such that the growth time scale of the instability $1/\sigma_f$ equals the diffusion time over δ , δ^2/D , which gives

$$\delta \sim 1.5 \left(\frac{D \eta_f}{\Delta \rho g} \right)^{1/3}. \quad (3)$$

In a system where the outer bath is much deeper than δ , the solute transport that the dissolution generates is always unstable and the onset of the instability corresponds to a constant value of the solutal Rayleigh number Ra_c [7,9,24]:

$$Ra_c = \frac{\Delta \rho g \delta^3}{D \eta_f}. \quad (4)$$

Solute diffusion and viscosity stabilize the interface and tend to increase the film thickness δ , while gravity drives the instability and tends to decrease δ . The mean viscosity η_f and density ρ_f inside the film depend on the concentration of the solute-laden fluid.

We observe in experiments that the dissolution rate reaches a stationary state, i.e., the mass fluxes balance. In one dimension, the conservation of mass in a stationary regime reads

$$-\rho_s \dot{h} = -D \frac{\partial C}{\partial x}(x) + C(x)[v(x) - \dot{h}], \quad (5)$$

where x is the normal distance from the solid interface and v the flow velocity in the laboratory frame (like \dot{h}). The diffusion coefficient D is taken constant. In the solution, the flow and the diffusion of the solute concentration balance the dissolution of the solid, which is made of one species only.

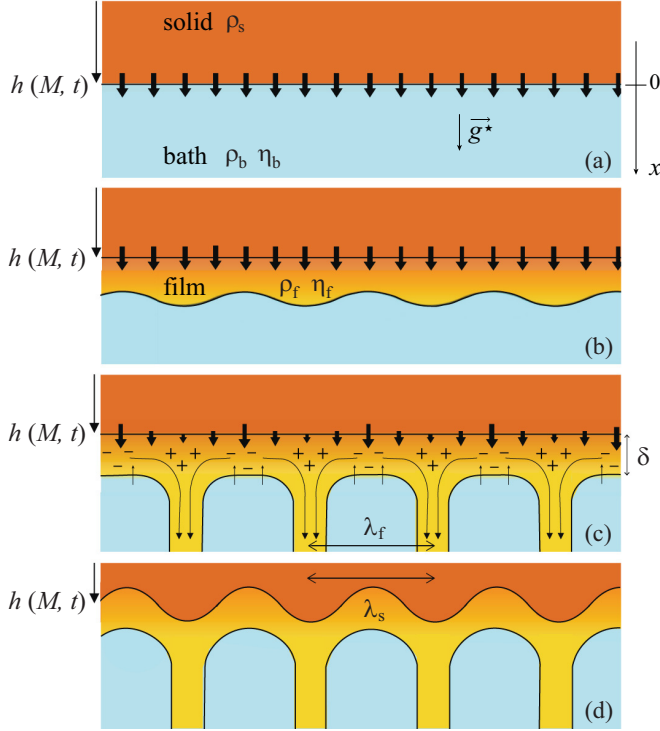


FIG. 7. Sketch of the first steps of the dissolution process in a transverse plane. Time increases from top to bottom. The instability selects the thickness of the concentration layer and the wavelength of solute threads. It produces a modulation of the solute concentration at the interface, which shapes the dissolving block. The concentration at the interface of the block is larger above a thread (+) than between threads (-). The block dissolves faster where the concentration at the interface is smaller [Eq. (1)].

At the solid interface, the solute transport is diffusion dominated, while it is advection dominated beyond the unstable solute layer, which gives three different equations for the dissolution flux:

$$-\rho_s \dot{h} = \alpha(C_{\text{sat}} - C_i) \quad (6)$$

$$\sim D \frac{(C_i - C_b)}{\delta} - \beta \dot{h} C_i \quad (7)$$

$$\sim \left(C_i - \frac{\rho_f - C_f}{\rho_b - C_b} C_b \right) \frac{4(\rho_f - \rho_b)g \cos \theta \delta^4}{3\eta_f \lambda_f^2}. \quad (8)$$

The first balance of solute flux per unit of surface is given by the kinetics of dissolution [Eq. (1)]. The second line is the diffusion-dominated flux of mass at the solid interface. At the interface, the flow does not penetrate the solid but the normal velocity is not necessarily zero, because the density of the solid and of the liquid may be different, $v(0) = \dot{h}(1 - \beta)$, where β is the ratio between the density of the solid and the density of the liquid at the interface ($\beta = \rho_s/\rho_l$). The gravity takes over the transport a distance δ from the solid interface within flowing threads with a wavelength λ_f (see Fig. 7). Thus, between threads and outside the mixture film, the concentration may be reduced to the one of the outer bath. The unstable solute layer assimilates to a boundary layer. Inside the boundary layer, the diffusion overcomes the advection so that the concentration decreases monotonically from the concentration C_i at the interface to the concentration C_b of the outer bath, almost linearly if D does not depend on C [24]. The concentration gradient at the interface scales like $(C_b - C_i)/\delta$.

The third line is the advection flux of mass at the boundary between the solute layer of thickness δ and the outer bath. It is buoyancy driven. The dissolution increases the concentration within the flowing film from the concentration of the outer bath C_b to the (mean) one of the film C_f . The scaling of the flow velocity corresponds to a two-dimensional lubrication flow of a fluid of density ρ_f and viscosity η_f inside a thin film of thickness δ confined between a rigid wall (the dissolving block) and an inviscid fluid of density ρ_b (the outer bath). The flow is driven by a characteristic pressure gradient $2\delta(\rho_b - \rho_i)g^*/\lambda_f$ and fed half a thread (see Fig. 7). Threads have a wavelength λ_f , which scales like δ [Eq. (2)]. g^* is the effective gravity for the growth of the instability. It should take into account the possible inclination of the dissolving interface. When the dissolving block makes an angle θ with the horizontal, $g^* = g \cos \theta$. It is the only way we take into account the inclination of the block, and we neglect the longitudinal flow. Between threads, a flow of the bath solution at concentration C_b renews the water inside the solute layer. The factor in front of C_b comes from the conservation of water inside the solute layer. This ratio is always close to 1. To obtain the scaling Eq. (8), we further assume that the thickness of threads is negligible compared to the distance λ_f between threads.

The equilibrium between the dissolution kinetics and the diffusive flux sets the concentration at the solid interface [Eqs. (6) and (7)]. The concentration C_i has two asymptotic expressions, depending on the ratio between the dissolution velocity α and the characteristic diffusion velocity over δ : D/δ . When the transport at the interface is limited by the diffusion, i.e., $D/(\alpha\delta) \ll 1$, the concentration at the interface is close to the saturation concentration. On the other hand, when the transport is limited by the dissolution kinetics, i.e., $D/(\alpha\delta) \gg 1$, the concentration at the interface is close to the concentration of the outer bath. For the dissolving materials we consider, the dissolution is limited by diffusion and we assume $C_i = C_{\text{sat}}$ (see the Supplemental Material [21,30,31]). The interested reader will find the scaling laws in the other limit in [24]. We assume a linear concentration profile in the mixture film so that the average concentration is $C_f = (C_{\text{sat}} + C_b)/2$. Finally, we assume a linear relationship between density and concentration, i.e., $\rho = \rho_0 + C(\rho_{\text{sat}} - \rho_0)/C_{\text{sat}}$, where ρ_0 is the density of the solution when $C = 0$. Then $\beta = \rho_s/\rho_{\text{sat}}$ and the density contrast reads $\rho_f - \rho_b = (\rho_{\text{sat}} - \rho_b)/2$. Combining Eqs. (7) and (8) gives

$$\delta \sim (3R_\lambda^2)^{1/3} \left[\frac{\rho_s}{\rho_s - \beta C_{\text{sat}}} \frac{D \eta_f}{(\rho_{\text{sat}} - \rho_b) g \cos \theta} \right]^{1/3} \left(\frac{C_{\text{sat}} - C_b}{C_{\text{sat}} - C_b \frac{\rho_{\text{sat}} - C_{\text{sat}}}{\rho_b - C_b}} \right)^{1/3} \quad \text{and} \quad (9)$$

$$\dot{h} \sim - \left(\frac{1}{3R_\lambda^2} \right)^{1/3} \left[\frac{D^2 (\rho_{\text{sat}} - \rho_b)^4 g \cos \theta}{\eta_f (\rho_s - \beta C_{\text{sat}})^2 \rho_s} \right]^{1/3} \frac{C_{\text{sat}}}{\rho_{\text{sat}} - \rho_0} \left(\frac{C_{\text{sat}} - C_b \frac{\rho_{\text{sat}} - C_{\text{sat}}}{\rho_b - C_b}}{C_{\text{sat}} - C_b} \right)^{1/3}, \quad (10)$$

where R_λ is the ratio between the wavelength λ_f of the buoyant instability and the thickness δ of the solute layer as given by the analysis of the Rayleigh-Taylor instability (for nondiffusing, homogeneous fluids) [27,29].

The instability of the flow naturally reflects on the field of concentration at the solid interface. Above the flowing thread, the concentration should be maximum and the solid dissolution rate should be minimum (see Fig. 7). The instability of the flow prints onto the solid, and we expect that the first observed wavelength of patterns at the solid interface corresponds to the wavelength of the flowing threads:

$$\lambda_s \sim (3R_\lambda^5)^{1/3} \left[\frac{\rho_s}{\rho_s - \beta C_{\text{sat}}} \frac{D \eta_f}{(\rho_{\text{sat}} - \rho_b) g \cos \theta} \right]^{1/3} \left(\frac{C_{\text{sat}} - C_b}{C_{\text{sat}} - C_b \frac{\rho_{\text{sat}} - C_{\text{sat}}}{\rho_b - C_b}} \right)^{1/3}. \quad (11)$$

Patterns grow because of a differential rate of dissolution imposed by a modulation of the solute concentration at the interface. The differential dissolution velocity should scale like the global

erosion velocity \dot{h} [24] so that the characteristic growth time T_s for the formation of patterns, i.e., to observe a given or detectable aspect ratio, should scale like λ_s/\dot{h} :

$$T_s \sim (9R_\lambda^7)^{1/3} \left[\frac{\eta_f^2 (\rho_s - \beta C_{\text{sat}}) \rho_s^2}{D (\rho_{\text{sat}} - \rho_b)^5 (g \cos \theta)^2} \right]^{1/3} \frac{\rho_{\text{sat}} - \rho_0}{C_{\text{sat}}} \left(\frac{C_{\text{sat}} - C_b}{C_{\text{sat}} - C_b \frac{\rho_{\text{sat}} - C_{\text{sat}}}{\rho_b - C_b}} \right)^{2/3}. \quad (12)$$

These scaling laws are somewhat different than the previous scalings [9,24,25]. Here, we derive the scaling laws from the conservation of mass, assuming a stationary dissolution flux, while previous scalings are based on a constant critical Rayleigh number [Eq. (4)], i.e., derived assuming that the thickness δ of the boundary layer is such that the system is at the instability threshold. The two differences are the terms $(\rho_s - \beta C_{\text{sat}})$ and $[C_{\text{sat}} - C_b(\rho_{\text{sat}} - C_{\text{sat}})/(\rho_b - C_b)]/(C_{\text{sat}} - C_b) \equiv \Omega$ in our scalings instead of ρ_s and 1, respectively, in previous scaling laws. The value of Ω increases with the bath concentration. It varies between 1 and 1.13 for salt and between 1 and 2 for caramel. This term does not change the quantitative values of the scaling laws very much. The term with the factor β depends on the dissolving material. For usual natural materials, which have a very low saturation concentration (i.e., $C_{\text{sat}} \ll \rho_{\text{sat}}$), the difference is incidental. It is not negligible for salt and caramel, for which β , C_{sat} , ρ_{sat} , and ρ_s are 1.96, 317 kg m⁻³, 1197 kg m⁻³, and 2348 kg m⁻³, and 1.06, 968 kg m⁻³, 1450 kg m⁻³, and 1540 kg m⁻³, respectively.

IV. RESULTS AND DISCUSSION

To calculate these scaling laws one has to choose values for the coefficient of diffusion D and for the viscosity η_f . We take the value of η_f that corresponds to the assumed mean concentration in the film, i.e., for $(C_{\text{sat}} + C_b)/2$. We measured the viscosity as a function of the solute concentration for solutions of caramel, saccharose, and salt (see Supplemental Material [21]). Because the saturation concentration of plaster in water is very weak, we take the viscosity of water for the plaster experiment. For D , we take the value that corresponds to the saturated concentration, i.e., the expected one at the block interface. It is determined from handbooks for salt and plaster and from the tabulated value at zero concentration for saccharose, which we extrapolate to the value at saturation using the Stokes-Einstein relation. See the Supplemental Material for values of these parameters [21]. These choices are not critical in the case of plaster, whose saturation concentration is very weak, and in the case of salt, for which D barely depends on concentration and the viscosity changes by a factor of 2 between the pure water and the saturated brine [32]. However, these choices are not insignificant in the case of caramel; the viscosity value of the saturated syrup is 4×10^4 times larger than the value of water. Most previous studies do not address the values of these coefficients, which is justified for materials with a small value of C_{sat} without impact on these parameters.

Figure 8 compares the experimental results to the scaling laws without prefactors, which include R_λ . The various dependencies of the erosion velocity and the initial wavelength of patterns with the density contrast, the block inclination, and, for caramel, the viscosity through the solute concentration are verified over several decades. We find a prefactor of about 0.18 for the dissolving velocity of salt blocks, which is very close to the expected order of magnitude [~ 0.29 with $R_\lambda = 3.8$, Eq. (10)]. For the dissolving velocity of caramel blocks the prefactor is larger and equals 2.7 when the expected one is about 0.34 (with $R_\lambda = 3$). The choices we do for the values of D and η_f may explain the different prefactors for experiments with salt and caramel. Note that the scaling laws compare well to the measurements, even if derived neglecting the solute flow along the dissolving block and the dynamics of patterns at the interface. Patterns are ignored, and the inclination of the block is taken into account only through the projection of the gravity, which gives good agreement with experimental data (Fig. 8). This is a noteworthy result for predictions in natural environments.

A horizontal interface dissolves faster than an inclined one. This result suggests that a polygonal or rounded object should not keep a constant shape while dissolving. This is different from recent observations of Davies Wykes *et al.*, who report that the gravity-driven dissolving velocity of a block does not depend on its inclination [10]. This may be ascribed to the limited range of their

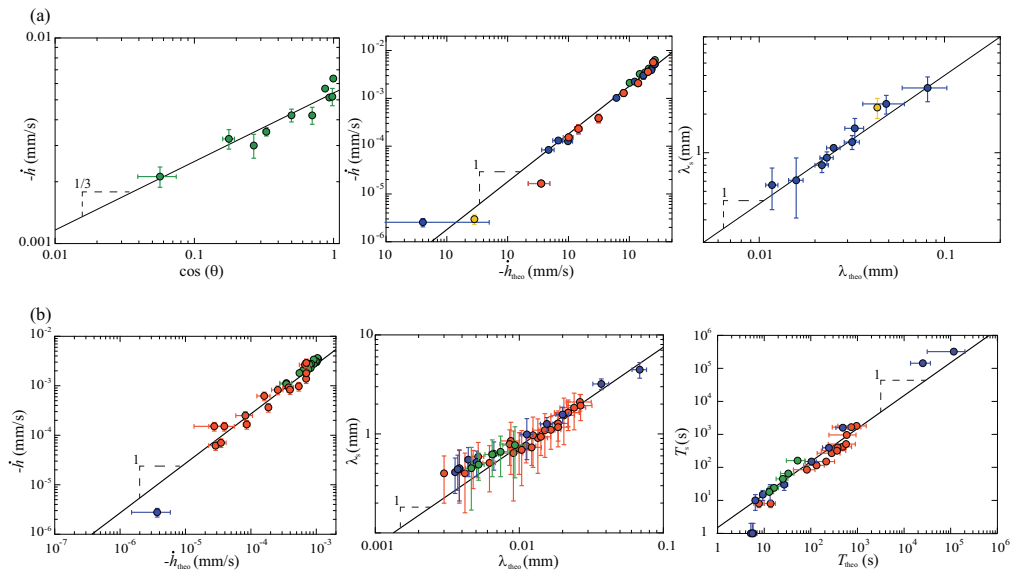


FIG. 8. Measurements of erosion velocity \dot{h} , first observed wavelengths of patterns λ_s , and growth characteristic time T_s as a function of scaling laws (without prefactor) for experiments with salt and plaster blocks (a) and with caramel blocks (b). Vertical and horizontal error bars show the resolution or dispersion of measurements and the scaling confidence interval due to parameter uncertainties, respectively. Colors stand for the varied parameter: (a) green— pure water with θ ranging between 6° and 87° ; orange— saline solutions of density ρ_b ranging between 1000 and 1189 kg m^{-3} and $\theta \simeq 30^\circ$; blue— saline solutions of density ρ_b ranging between 997 and 1197 kg m^{-3} , and various inclinations θ . The yellow point corresponds to gypsum into pure water with $\theta \simeq 52^\circ$. The line in the first graphic shows a power law with an exponent $1/3$. The lines in the two other graphics show relations of proportionality with constants equal to 0.2 for \dot{h} and 42 for λ_s . (b) \dot{h} graphic: green— pure water with θ ranging between 0 and 88° ; orange— sucrose solution with density ρ_b ranging between 1000 and 1320 kg m^{-3} and $\theta \simeq 73^\circ$ – 75° ; blue— caramel solution with density $\rho_b = 1403 \text{ kg m}^{-3}$ and $\theta = 75^\circ$. (b) λ_s and T_s graphics: green— sucrose solution of density $\rho_b = 1150 \text{ kg m}^{-3}$ with θ ranging between 45° and 85° ; orange— sucrose solution with density ρ_b ranging between 1000 and 1320 kg m^{-3} and $\theta \simeq 73^\circ$ – 77° , blue— caramel solution with density ρ_b ranging between 1000 and 1430 kg m^{-3} and $\theta \simeq 70^\circ$ – 75° . The coefficient of proportionality of black lines are 2.7 for \dot{h} , 75 for λ_s , and 1.5 for T_s . The Supplemental Material shows tables and plots of the raw data [21].

experiments and the weak dependency at small angles [$-\dot{h} \propto \cos^{1/3} \theta$, Eq. (10)] and/or to the relative small size of objects they consider. The instability fully develops after an entry length (see Fig. 2), and the differences in macroscopic receding velocity should affect the overall shape of the object if the latter is way larger than the size of patterns.

Our experiments where blocks are inclined clearly show a characteristic wavelength for the initial stripes that longitudinally extend all along the block. The initial wavelength of patterns we measure agree with the scaling law of the most unstable wavelength of the flow instability [Fig. 8, Eq. (11)]. Like for the erosion velocity, the observed prefactor is closer for experiments with salt (~ 40 instead of ~ 13) than for experiments with caramel (~ 75 instead of ~ 8.8). Note that measurements may deviate from the scaling law at small values. However, this could be ascribed to experimental issues like an initial roughness of the solid surface or to the difficulty of measuring the very first wavelength when the patterns evolve rapidly.

Figure 8 shows that the characteristic growth time of patterns on caramel blocks properly scales like λ_s/\dot{h} [Eq. (12)]. This raises the question of the pattern growth rate. Most of instabilities grow exponentially at first in the linear regime. An exponential growth demands a coupling between the

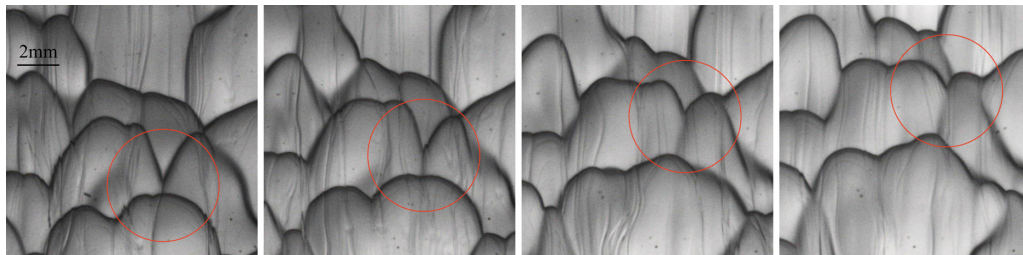


FIG. 9. Pattern dynamics. Bottom view of a caramel block dissolving into water. A V-shape pointing downstream vanishes. The block makes an angle of 60° with the horizontal. Gravity points towards the bottom of images. There is a 6-min time delay between snapshots. First image is taken 80 min after immersion.

cause and the effect. Such a coupling is not obvious here where the patterning of the block comes from the buoyant instability of the dissolution flow. However, the flow instability can imprint onto the dissolving solid only if the positions of flowing threads are stabilized. A possible interaction between the patterns and the flow could rely on the spatial stabilization of dissolution plumes. The position of plumes may be all the more stable (stationary) that a dissolution peak is developed overhead. It is worth noting that the wavelength of initial patterns does not seem as well defined as in our experiments with inclined blocks when interfaces are horizontal [9]. In our experiments, the dissolution flow along the block could stabilize the transverse position of early plumes and limit their interactions. Indeed, the longitudinal extension of early stripes is striking (Fig. 6). Note that an outer flow, transverse to the growth direction of the instability, reduces the flow pattern to two dimensions (longitudinal rolls) in Rayleigh-Bénard experiments with small gaps [33,34]. In our experiments the transverse-to-growth-direction flow is the dissolution flow along the inclined block itself. It is the opposite case of the Rayleigh-Bénard vortices in granular flows, where it is the flow that “heats” the granular medium [35]. Anyway, without coupling between the amplitude of stripes and their growth velocity, the amplitude of early stripes would grow linearly in time. Numerical simulations could address this question effectively.

We observe experimentally that the initial longitudinal stripes do not last and turn into scalloped patterns that deepen, enlarge, elongate, and propagate upstream. This is definitely a true interaction between the patterns and the dissolution flow. Figure 1 shows that solute plumes preferentially detach the boundary layer from peaks. This explains the upstream propagation of patterns, the reorientation of stripes, and the final concave shape of scallops with acute peaks and rounded troughs as shown in Fig. 5. The buoyancy-driven dissolution tends to form and preserves singularities. Following the solute flow along the solid interface, the concentration is larger, closer to the saturation value, and the concentration gradient is smaller because of a thicker boundary layer upstream from the peak, before the plume detaches, than downstream. Thus, near a peak where a plume detaches, the dissolution flux is larger downstream than upstream from the peak. This differential dissolution enforces the peak (and patterns) to propagate upstream. Because crests channelize the solute flow, the initial longitudinal stripes are unstable. The propagation velocity is maximum where plumes detach because the spatial variation of the solute flux is maximum there. If we consider, for example, that a stripe is not perfectly longitudinal but makes a small angle with the downstream flow, it will break and reorient where plumes detach because of an inhomogeneous propagation velocity. The image sequence shown in Fig. 9 illustrates the propensity of patterns to orient transversally.

V. ANALOGY WITH THE FORMATION OF PENITENTES AND SUBLIMATION PATTERNS

Penitentes are ice or snow spikes that form on high-altitude glaciers in sublimation conditions and have recently been suspected on other planetary bodies [36,37]. They point in the direction of the

sun, which suggests that the sublimation is driven by the heat flux resulting from the light absorption by the ice. Previous studies proposed a coupling between the ice topography and the sublimation rate to explain the pattern formation [38–42]. Because of a curvature effect, a trough receives more light than a peak and a perturbation of the topography grows. The corresponding linear stability analysis, where heat and mass diffuse but without advection, does not predict the selection of an initial wavelength [42]. Claudin *et al.* propose that the wavelength may be selected by the boundary layer of an external air flow above the ice surface [42]. However, Bergeron *et al.* report that an air flow above the snow surface prevents the formation of penitentes in their experiment [43].

We propose that penitentes first form by differential sublimation because of a buoyancy instability in the flow of moist air above the ice surface, like for the dissolution patterns we report. The initial ice peaks would then not form because of the coupling between the topography and the radiative heat flux but would simply be a print of the air flow instability. The buoyancy instability would be driven by moisture, because moist air is lighter than dry air.

The ice sublimates because the partial pressure of water vapor in the air is lower than the equilibrium vapor pressure. At the ice interface, the air is almost saturated in water vapor with a concentration C_{sat} , which depends on the temperature. The incident light brings energy to sublimate the ice but also to heat the (moist) air at the ice interface. The warming of air at the ice interface enhances the instability, because the equilibrium vapor pressure of water in the air increases with temperature and so does the buoyancy. Thereby, the energy balance must be resolved concurrently with the equations of mass conservation. The incident light brings a characteristic heat flux, which is absorbed by the ice. In a steady state of sublimation, the absorbed heat at the interface diffuses in the ice, diffuses and convects in the air, and provides the energy for the sublimation. The balance between the sublimation fluxes derived from the conservation of mass and derived from the conservation of energy would allow the sublimation rate, the thickness of the buoyancy unstable layer of moist air (and the wavelength between threads), together with the temperature of the air at the ice/air interface to be calculated.

A full analysis of this problem is beyond the scope of our article. However, we can estimate the first wavelength of buoyancy-driven penitentes for given temperatures of the moist air layer and of the dry ambient air, which set the values of parameters like the saturation concentration of the water vapor. For a dry atmosphere at -20°C , if the ice interface is heated up to -5°C , we find $\lambda_s \simeq 32$ mm according to Eq. (11), with the prefactor we measure for salt dissolution (see Fig. 8).¹ It compares to the typical centimeter scale observed in experiments [43]. Although it might be annihilated in windy conditions, the buoyancy-driven sublimation and evaporation might make non-negligible contributions to water budgets [44–47].

VI. CONCLUSION, FREE CONVECTION, AND PATTERNS IN NATURAL ENVIRONMENTS

Our experimental observation of dissolution of various solids in aqueous solutions evidences the succession of two pattern formation mechanisms. First, a longitudinal instability develops with the appearance of stripes carved on the surface and spaced out by a well-defined wavelength. We source it to the buoyancy hydrodynamical instability due to the density stratification that the dissolution generates. It ends up to the emission of solute plumes spatially separated. We show that the inclination of the dissolving blocks stabilizes the location of the plumes in order to print coherently the block surface. We confirm that this observed primary pattern follows scaling laws based on the hydrodynamics only. At later times the stripes eventually turn into scallops. This second mechanism involves strong interactions between the flow and the topography. The final shape displays very stereotyped scallops, similar to some observed in nature, advocating for the importance of the role played by buoyancy in natural systems.

¹This value corresponds to $D = 2.14 \times 10^{-5} \text{ m}^2 \text{ s}^{-1}$, $\eta_f = 1.65 \times 10^{-5} \text{ Pa s}$, $\rho_{\text{sat}} = 1.314 \text{ kg m}^{-3}$, $\rho_b = 1.394 \text{ kg m}^{-3}$.

Underground cavities shaped by free convection in nature are reported in several environments, including salt, gypsum, and limestone rocks. They occur as dissolutional chambers or vertical breakdown structures and are confined systems [48]. The dissolutional chambers develop upwards, and the buoyancy-driven flow shapes the cavity into an upside-down triangular prism or cone with a flat horizontal ceiling [49]. This particular shape is another indication that free convection increases the dissolution rate. Onto the top walls, centimeter cups with sharp edges named dissolution pits are observed [50,51]. In our experiments with inclined blocks, the morphology of the dissolution pits is reminiscent of the scalloplike patterns observed in unconfined systems such as caves or icebergs. However, these last patterns are likely produced by the turbulent flow of a ground river or an ocean current. An externally imposed flow should prevail on the buoyancy to drive the dissolution when the turbulence of the flow decreases the thickness of the concentration boundary layer below the one imposed by the solutal Rayleigh-Bénard instability [Eqs. (3) and (9)]. Regarding heat transfer, numbers of studies address these questions [52,53].

Scallops shaped by an external flow have been successfully reproduced in laboratory flumes with a turbulent flow over beds of plaster [54–56] or ice [57–59]. These studies report that mature patterns in experiments have constant amplitude and longitudinal wavelength (periodicity in the stream direction), which scale as one over the flow velocity. In the field, scallops could thus be used as proxies of the flow [60,61]. Theoretically, Hanratty and Claudin *et al.* studied the pattern formation on a bed sheared by a turbulent flow in the limit of deep flows [62,63]. Patterns arise from the coupling between the dissolving topography and the turbulent viscosity at the solid interface, which increases the solute transport [63]. Interestingly, the positive feedback is restricted to small values of the hydrodynamic roughness of the flow and to a narrow range of wavelengths which scale as one over the characteristic velocity of the flow [62,63]. Considering the relative small aspect ratios of scallops observed in experiments and in the field, this result obtained in the linear regime could explain the longitudinal wavelengths and amplitudes of mature scallops. The three-dimensional shape of these scallops remains an open question. In our experiments, the convective solute flow driven by the dissolution of inclined blocks shapes bedforms through differential dissolution. Initial bedforms are longitudinal ridges which turn into three-dimensional scalloplike patterns. Unlike the scallops in turbulent flows, the amplitude, width, and length of the free dissolution scallops are not constant nor do they saturate in our experiments but increase with time. Moreover, the free dissolution scallops propagate upstream, while scallops in turbulent flow propagate downstream [54–56,59,60]. This difference in propagation direction reflects a different shift between the topography and the erosion rate. The erosion must be maximum on the lee side of free dissolution scallops and on the stoss side of scallops in a turbulent flow. If these last ones propagate downstream but do not grow in size, the erosion is maximum at midslope. Despite the different space shifts between the erosion rate and the topography, these two patterns look similar. They exhibit sharp peaks and asymmetric profiles with a larger slope on the lee side than on the stoss side. The peaks may, however, be more acute in our experiments, with a rather concave shape upstream, while the stoss side of the peaks appear more rounded in flow experiments [54,55,60]. The overall resemblance between in flow and free dissolution scallops incites one to link some aspects of their morphogenesis. In both cases, the transverse topography could be due to an instability in the dissolution flow only, while a true feedback between the topography and the solute flow should be responsible for the longitudinal topography. The first observed patterns could be longitudinal ridges in both cases, and they could trigger the transverse instability.

ACKNOWLEDGMENTS

We thank Cyril Ozouf, who did some experiments during an internship in our laboratory, and Marc Durand for fruitful discussions. We thank Jérôme Jovet for his help to do Schlieren imaging and Imane Boucenna for sharing her rheometer. This research was funded by the french Agence Nationale de la Recherche (Grants No. ANR-12-BS05-0001/EXO-DUNES and No. ANR-16-CE30-0005/ERODISS).

- [1] C. Cohen, M. Berhanu, J. Derr, and S. Courrech du Pont, Erosion patterns on dissolving and melting bodies, *Phys. Rev. Fluids* **1**, 050508 (2016).
- [2] J. Schürr, Sur la vitesse de dissolution des sels dans leurs solutions aqueuses (dissolution rate of salts in aqueous solutions), *J. Phys. Théor. Appl.* **4**, 17 (1905).
- [3] F. Garner and J. Hoffman, Mass transfer from single solid spheres by free convection, *AIChE J.* **7**, 148 (1961).
- [4] D. G. Thomas and R. A. Armistead, Concentration-gradient-driven convection: Experiments, *Science* **160**, 995 (1968).
- [5] H. Grijseels, D. Crommelin, and C. De Blaey, Hydrodynamic approach to dissolution rate, *Pharm. Weekbl.* **3**, 1005 (1981).
- [6] D. Hurlle, E. Jakeman, and A. Wheeler, Effect of solutal convection on the morphological stability of a binary alloy, *J. Cryst. Growth* **58**, 163 (1982).
- [7] S. Tait and C. Jaupart, Compositional convection in viscous melts, *Nature (London)* **338**, 571 (1989).
- [8] R. Kerr, Melting driven by vigorous compositional convection, *J. Fluid Mech.* **280**, 255 (1994).
- [9] T. S. Sullivan, Y. Liu, and R. E. Ecke, Turbulent solutal convection and surface patterning in solid dissolution, *Phys. Rev. E* **54**, 486 (1996).
- [10] M. S. Davies Wykes, J. M. Huang, G. A. Hajjar, and L. Ristroph, Self-sculpting of a dissolvable body due to gravitational convection, *Phys. Rev. Fluids* **3**, 043801 (2018).
- [11] J. A. Neufeld, M. A. Hesse, A. Riaz, M. A. Hallworth, H. A. Tchelepi, and H. E. Huppert, Convective dissolution of carbon dioxide in saline aquifers, *Geophys. Res. Lett.* **37**, L22404 (2010).
- [12] H. E. Huppert and J. A. Neufeld, The fluid mechanics of carbon dioxide sequestration, *Annu. Rev. Fluid Mech.* **46**, 255 (2014).
- [13] V. Loodts, C. Thomas, L. Rongy, and A. De Wit, Control of Convective Dissolution by Chemical Reactions: General Classification and Application to CO₂ Dissolution in Reactive Aqueous Solutions, *Phys. Rev. Lett.* **113**, 114501 (2014).
- [14] A. C. Slim, Solutal-convection regimes in a two-dimensional porous medium, *J. Fluid Mech.* **741**, 461 (2014).
- [15] S. Tait and C. Jaupart, Compositional convection in a reactive crystalline mush and melt differentiation, *J. Geophys. Res.* **97**, 6735 (1992).
- [16] P. Meakin and B. Jamtveit, Geological pattern formation by growth and dissolution in aqueous systems, *Proc. R. Soc. London, Ser. A* **466**, 659 (2010).
- [17] L. Solari and G. Parker, Morphodynamic modeling of the basal boundary of ice cover on brackish lakes, *J. Geophys. Res.: Earth Surf.* **118**, 1432 (2013).
- [18] See Supplemental Material at <http://link.aps.org/supplemental/10.1103/PhysRevFluids.5.053802> for a Schlieren imaging movie of a salt block dissolving into water.
- [19] See Ref. [18] for a time lapse of the pattern formation and evolution of a caramel block dissolving into water.
- [20] B. Favier, J. Purseed, and L. Duchemin, Rayleigh-Bénard convection with a melting boundary, *J. Fluid Mech.* **858**, 437 (2019).
- [21] See Ref. [18] for tables and plots of the raw data and an explanation of the diffusion-limited dissolution regime.
- [22] A. C. Lasaga, *Kinetic Theory in the Earth Sciences* (Princeton University Press, Princeton, NJ, 2014).
- [23] J. Crank, *The Mathematics of Diffusion* (Clarendon Press, Oxford, 1975).
- [24] J. Philippi, M. Berhanu, J. Derr, and S. Courrech du Pont, Solutal convection induced by dissolution, *Phys. Rev. Fluids* **4**, 103801 (2019).
- [25] R. Kerr, Dissolving driven by vigorous compositional convection, *J. Fluid Mech.* **280**, 287 (1994).
- [26] F. Haudin, L. Riolfo, B. Knaepen, G. Homsy, and A. de Witt, Experimental study of a buoyancy-driven instability of a miscible horizontal displacement in a Hele-Shaw cell, *Phys. Fluids* **26**, 044102 (2014).
- [27] H. Brown, Rayleigh-Taylor instability in a finite thickness layer of a viscous fluid, *Phys. Fluids A* **1**, 895 (1988).
- [28] L. Limat, Instability of a liquid hanging below a solid ceiling: Influence of layer thickness, *C. R. Acad. Sci. Paris* **317**, 563 (1993).

- [29] J. Lister and R. Kerr, The effect of geometry on the gravitational instability of a buoyant region of viscous fluid, *J. Fluid Mech.* **202**, 577 (1989).
- [30] M. Alkattan, E. H. Oelkers, J.-L. Dandurand, and J. Schott, Experimental studies of halite dissolution kinetics, 1. The effect of saturation state and the presence of trace metals, *Chem. Geol.* **137**, 201 (1997).
- [31] J. Colombani and J. Bert, Holographic interferometry study of the dissolution and diffusion of gypsum in water, *Geochim. Cosmochim. Acta* **71**, 1913 (2007).
- [32] V. Vitagliano and P. A. Lyons, Diffusion coefficients for aqueous solutions of sodium chloride and barium chloride, *J. Am. Chem. Soc.* **78**, 1549 (1956).
- [33] R. Kelly, The onset and development of thermal convection in fully developed shear flows, in *Advances in Applied Mechanics* (Elsevier, New York, 1994), Vol. 31, pp. 35–112.
- [34] H. Pabiau, S. Mergui, and C. Benard, Wavy secondary instability of longitudinal rolls in Rayleigh–Bénard–Poiseuille flows, *J. Fluid Mech.* **542**, 175 (2005).
- [35] Y. Forterre and O. Pouliquen, Longitudinal Vortices in Granular Flows, *Phys. Rev. Lett.* **86**, 5886 (2001).
- [36] J. Moores, C. Smith, A. Tigo, and S. Guzewich, Penitentes as the origin of the bladed terrain of tartarus dorsa on pluto, *Nature (London)* **541**, 188 (2017).
- [37] D. Hobley, J. Moore, A. Howard, and O. Umurhan, Formation of meter-scale bladed roughness on Europa’s surface by ablation of ice, *Nat. Geosci.* **11**, 901 (2018).
- [38] L. Lliboitry, The origin of penitentes, *J. Glaciol.* **2**, 331 (1954).
- [39] M. D. Betterton, Theory of structure formation in snowfields motivated by penitentes, suncups, and dirt cones, *Phys. Rev. E* **63**, 056129 (2001).
- [40] T. Bartels-Raush, V. Bergeron, J. H. E. Cartwright, R. Escibano, J. L. Finney, H. Grothe, P. J. Gutiérrez, J. Haapala, W. F. Kuhs, J. B. C. Pettersson *et al.*, Ice structures, patterns, and processes: A view across the ice fields, *Rev. Mod. Phys.* **84**, 885 (2012).
- [41] L. M. Cathles, D. S. Abbot, and D. R. MacAyeal, Intra-surface radiative transfer limits the geographic extent of snow penitents on horizontal snowfields, *J. Glaciol.* **60**, 147 (2014).
- [42] P. Claudin, H. Jarry, G. Vignoles, M. Plapp, and B. Andreotti, Physical processes causing the formation of penitentes, *Phys. Rev. E* **92**, 033015 (2015).
- [43] V. Bergeron, C. Berger, and M. D. Betterton, Controlled Irradiative Formation of Penitentes, *Phys. Rev. Lett.* **96**, 098502 (2006).
- [44] N. Shahidzadeh-Bonn, S. Rafai, A. Azouni, and D. Bonn, Evaporating droplets, *J. Fluid Mech.* **549**, 307 (2006).
- [45] S. Dehaeck, A. Rednikov, and P. Colinet, Vapor-based interferometric measurement of local evaporation rate and interfacial temperature of evaporating droplets, *Langmuir* **30**, 2002 (2014).
- [46] O. Carrier, N. Shahidzadeh-Bonn, R. Zargar, M. Aytouna, M. Habibi, J. Eggers, and D. Bonn, Evaporation of water: Evaporation rate and collective effects, *J. Fluid Mech.* **798**, 774 (2016).
- [47] B. Dollet and F. Boulogne, Natural convection above circular disks of evaporating liquids, *Phys. Rev. Fluids* **2**, 053501 (2017).
- [48] A. B. Klimchouk, *Hypogene Speleogenesis: Hydrogeological and Morphogenetic Perspective*, Special Paper no. 1 (National Cave and Karst Research Institute, Carlsbad, NM, 2007), p. 106.
- [49] D. Gechter, P. Huggenberger, P. Ackerer, and H. N. Waber, Genesis and shape of natural solution cavities within salt deposits, *Water Resour. Res.* **44**, W11409 (2008).
- [50] S. Kempe, Cave genesis in gypsum with particular reference to underwater conditions, *Cave Science* **49**, 1 (1972).
- [51] S. Kempe, Gypsum karst of Germany, *Int. J. Speleology* **25**, 16 (1996).
- [52] T. L. Bergman, F. P. Incropera, A. S. Lavine, and D. P. DeWitt, *Introduction to Heat Transfer* (John Wiley & Sons, New York, 2011).
- [53] S. Pirozzoli, M. Bernardini, R. Verzicco, and P. Orlandi, Mixed convection in turbulent channels with unstable stratification, *J. Fluid Mech.* **821**, 482 (2017).
- [54] J. Allen, Bed forms due to mass transfer in turbulent flows: A kaleidoscope of phenomena, *J. Fluid Mech.* **49**, 49 (1971).
- [55] P. N. Blumberg and R. L. Curl, Experimental and theoretical studies of dissolution roughness, *J. Fluid Mech.* **65**, 735 (1974).

- [56] B. Villien, Y. Zheng, and D. Lister, Surface dissolution and the development of scallops, *Chem. Eng. Commun.* **192**, 125 (2005).
- [57] G. D. Ashton and J. F. Kennedy, Ripples on underside of river ice covers, *J. Hydraul. Div.* **98**, 1603 (1972).
- [58] R. R. Gilpin, T. Hirata, and K. C. Cheng, Wave formation and heat transfer at an ice-water interface in the presence of a turbulent flow, *J. Fluid Mech.* **99**, 619 (1980).
- [59] M. Bushuk, D. M. Holland, T. P. Stanton, A. Stern, and C. Gray, Ice scallops: A laboratory investigation of the ice–water interface, *J. Fluid Mech.* **873**, 942 (2019).
- [60] R. L. Curl, Scallops and flutes, *Transactions Cave Research Group of Great Britain* **7**, 121 (1966).
- [61] R. L. Curl, Deducing flow velocity in cave conduits from scallops, *NSS Bull.* **36**, 1 (1974).
- [62] T. J. Hanratty, Stability of surfaces that are dissolving or being formed by convective diffusion, *Annu. Rev. Fluid Mech.* **13**, 231 (1981).
- [63] P. Claudin, O. Durán, and B. Andreotti, Dissolution instability and roughening transition, *J. Fluid Mech.* **832**, R2 (2017).

Correction: The parameter β was found to be in error and related terms have been fixed in text after Eq. (8) and before Eq. (9) and Sec. IV, necessitating a replacement of Fig. 8.